

Cite this: *Lab Chip*, 2011, **11**, 912

www.rsc.org/loc

PAPER

## Deformability-based cell classification and enrichment using inertial microfluidics†

Soojung Claire Hur,<sup>ae</sup> Nicole K. Henderson-MacLennan,<sup>b</sup> Edward R. B. McCabe<sup>c</sup> and Dino Di Carlo<sup>\*de</sup>

Received 12th November 2010, Accepted 6th January 2011

DOI: 10.1039/c0lc00595a

The ability to detect and isolate rare target cells from heterogeneous samples is in high demand in cell biology research, immunology, tissue engineering and medicine. Techniques allowing label-free cell enrichment or detection are especially important to reduce the complexity and costs towards clinical applications. Single-cell deformability has recently been recognized as a unique label-free biomarker for cell phenotype with implications for assessment of cancer invasiveness. Using a unique combination of fluid dynamic effects in a microfluidic system, we demonstrate high-throughput continuous label-free cell classification and enrichment based on cell size and deformability. The system takes advantage of a balance between deformability-induced and inertial lift forces as cells travel in a microchannel flow. Particles and droplets with varied elasticity and viscosity were found to have separate lateral dynamic equilibrium positions due to this balance of forces. We applied this system to successfully classify various cell types using cell size and deformability as distinguishing markers. Furthermore, using differences in dynamic equilibrium positions, we adapted the system to conduct passive, label-free and continuous cell enrichment based on these markers, enabling off-chip sample collection without significant gene expression changes. The presented method has practical potential for high-throughput deformability measurements and cost-effective cell separation to obtain viable target cells of interest in cancer research, immunology, and regenerative medicine.

### Introduction

Alteration in the deformability (or mechanical strength) of single cells has been identified to be a useful indicator of changes in cellular phenotype of importance for biological research. Various diseases are associated with cell deformability alterations including cancer,<sup>1–4</sup> blood diseases (sickle cell anemia, hereditary spherocytosis, and immune haemolytic anaemia),<sup>5,6</sup> and inflammation.<sup>7,8</sup> In particular, the stiffness of individual cancer cells has been found to be drastically reduced when compared to normal tissue of the same origin. Furthermore, decreasing single-cell stiffness was correlated with increasing invasiveness or metastatic potential. Biomechanical assays confirmed this correlation both with *in vitro* human cancer cell lines as well as clinical biopsies.<sup>1–4</sup> These results are practically important considering

the simplicity and low potential cost for obtaining label-free biophysical measurements. A label-free deformability biomarker would likely have lower operating costs than current molecular-based biomarkers that require pre-processing steps, dyes, and/or costly antibodies. Furthermore, disease states of interest can be expanded to those without predetermined immunological markers as long as a correlation between deformability phenotype and clinical outcome is confirmed. Specifically, deformability-based target cell classification/enrichment would be useful for cancer research and diagnostics since it would enable controlled experiments correlating cell mechanics of cancer cell lines with known genetic defects as well as analysis of malignant cells of unknown origin (*e.g.* circulating tumor cells (CTCs) in peripheral blood or malignant cells in biopsy samples) for cancer staging, relapse detection, molecular analysis of cancer drug resistance, and potentially early detection.<sup>1,3,4,9</sup>

Current techniques developed for measuring deformability and elastic properties of cells include micropipette aspiration,<sup>10–12</sup> atomic force microscopy,<sup>4,13,14</sup> optical deformability,<sup>3</sup> magnetic bead twisting assays<sup>15</sup> and optical tweezers.<sup>2</sup> Despite the success in obtaining overall deformability measurements for cells of interest, the low throughput (1 cell min<sup>-1</sup> to 1 cell s<sup>-1</sup>) of current cell deformability measurement techniques renders current technologies ill-suited for statistical analysis of large heterogeneous biological samples or rare cell detection. For example, current throughput does not allow routine screening of millions

<sup>a</sup>Department of Mechanical and Aerospace Engineering, University of California, Los Angeles, Los Angeles, CA, 90095, USA

<sup>b</sup>Department of Pediatrics, University of California, Los Angeles, Los Angeles, CA, 90095, USA

<sup>c</sup>Linda Crnic Institute for Down Syndrome and Department of Pediatrics, University of Colorado School of Medicine, Aurora, CO, 80045, USA

<sup>d</sup>Department of Bioengineering, University of California, Los Angeles, Los Angeles, CA, 90095, USA. E-mail: dicarlo@seas.ucla.edu; Tel: +1 310 983 3235

<sup>e</sup>California NanoSystems Institute, Los Angeles, CA, 90095, USA

† Electronic supplementary information (ESI) available: ESI\_Figure 1–7 and ESI\_Movie. See DOI: 10.1039/c0lc00595a

of cells, which is often desired for statistically robust diagnostic and research applications (*e.g.* detection/enumeration of cancer cells in blood or biopsies). Moreover, post-measurement enrichment of cell populations with uniform deformability has not been demonstrated for current technologies although high-purity isolation of viable cells with preserved gene expression profiles would facilitate the comprehensive assessment of single-cell mechanics correlated with unexplored genes responsible for such changes in phenotype. Therefore, novel techniques allowing deformability activated target cell enrichment and/or high-throughput deformability measurement of individual cells would expand the research use and clinical adoption of this biomarker.

In order to address the limited throughput and off-chip viable sample collection of current techniques, we present a passive label-free cell classification and enrichment technique utilizing intrinsic properties of living cells (*i.e.* size and deformability). The system employs inertial focusing in combination with deformability-induced migration to identify and separate more deformable cells of interest in a label-free, continuous flow, and high-throughput manner. The microfluidic system operates by yielding unique equilibrium positions in a channel cross-section for flowing particles with heterogeneous size/deformability. First, to systematically investigate the effect of particle deformability on our measurements and to calibrate our system we evaluated the unique focusing behavior for silicone oil droplets over a range of viscosities. Then, we applied the system to assay a large variety of blood cells and cultured cell lines. Furthermore, as a proof-of-concept towards analysis of CTCs from blood, cancer cells, spiked in a dilute blood sample prior to the injection, were separated and enriched using our approach. Viability and global gene expression of the collected cells were examined in order to determine whether the proposed fluidic process adversely affects processed cells. Taking advantage of microscale physics, the presented method provides a simple target cell classification and enrichment approach for a variety of applications where deformability and size are suitable biomarkers.

## Theoretical background: Inertial focusing of deformable particles in poiseuille flow

Inertial effects in microfluidic systems have recently been gaining much attention because of the ability to easily focus and order particles and cells continuously without external forces.<sup>16</sup> In brief, an inertial lift force,  $F_L$ , induces lateral migration of particles in confined flow (see Fig. 1) and creates distinct inertial lift focusing positions at finite particle Reynolds number,<sup>17</sup>  $R_p = \frac{\rho_{ex} U_{max} a^2}{\mu_{ex} D_h} = R_c \left( \frac{a}{D_h} \right)^2$ . Here,  $\rho_{ex}$ ,  $U_{max}$ ,  $\mu_{ex}$ ,  $R_c$ ,  $a$  are the density, the maximum velocity, the dynamic viscosity of the continuous phase fluid, the channel Reynolds number, and the particle diameter, respectively, while  $D_h$  is the hydraulic diameter of the channel, defined as  $D_h = \frac{2WH}{W+H}$  where  $W$  and  $H$  are the channel width and height, respectively. Particularly relevant to this work, we have previously demonstrated that particles/cells can be inertially focused at two distinct lateral focusing positions and one uniform  $z$ -position using high aspect ratio channels ( $2 < H/W$ ).<sup>18</sup> These channels reduced the probability of particle overlap and out-of-focus blur and provided

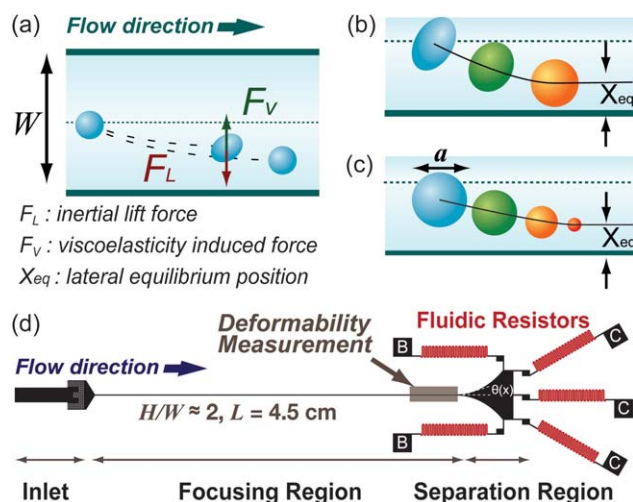


**Fig. 1** Classifying and separating cells and particles by deformability. (a) The balance between two lateral forces, namely inertial lift force,  $F_L$ , and viscoelasticity induced force,  $F_V$ , leads to unique lateral inertial focusing equilibrium positions,  $X_{eq}$ , for (b) deformable particles and (c) rigid particles with various diameters,  $a$ . (d) The microfluidic device used for cancer cell enrichment based on these parameters consists of an inlet with a coarse filter, a straight focusing ( $40 \times 93 \mu\text{m}$ ) region, and a gradually expanding separation region ending in 5 branched outlets with high fluidic resistance. Outlets, denoted as B or C, represent the designated collection outlets for blood cells and cancer cells, respectively in enrichment experiments. All schematics represent the top view of the microfluidic device.

similar cell signature images, allowing accurate cell-type classification with extreme throughput. These high-aspect ratio channel structures are used to focus cells to two lateral positions in this work.

In addition to nonlinearity associated with the inertia of the fluid, nonlinear lateral migration can occur when the particle itself is deformable. Early theoretical investigations reported that elastic solid particles experience a force away from the wall in Poiseuille flow,<sup>19</sup> such that particles laterally migrated to the channel centerline, even in the zero-Reynolds-number limit.<sup>19,20</sup> Following these works, several theoretical, numerical and a few experimental studies expanded the investigation of this phenomenon to consider the motion of bubbles, liquid drops, vesicles and viscous capsules surrounded by elastic membranes, flowing in wall-bounded flows.<sup>19–24</sup> Lateral migration of deformable particles was found to result from a nonlinearity caused by matching of velocities and stresses at the particle/droplet interface.<sup>24</sup> That is, the magnitude of lateral drift velocity and lift force is closely related to the deformed shape of the object. For droplets with surface tension,  $\sigma$ , the Weber,  $We = \frac{\rho_{ex} U_{max}^2 a}{\sigma}$ , or capillary,  $Ca = \frac{\mu_{ex} U_{max} a}{\sigma W}$  number provides a dimensionless parameter (inertial stress vs. surface tension or viscous stress vs. surface tension) that characterizes the relative deformation expected for a droplet.<sup>25</sup> The internal-to-external viscosity ratio,  $\lambda = \mu_{in}/\mu_{ex}$ , is another significant parameter characterizing droplet deformation and drift.<sup>21,22,24,25</sup> The drift velocity (*i.e.*, lift force) was found to increase with the droplet deformability and the direction of migration is predominantly toward the channel centerline for all deformable

objects. A notable exception to this trend, and migration towards the wall, was observed with viscous droplets when the viscosity ratio ranged between 0.5 and 10.<sup>22,24,25</sup>

The fact that deformable particles experience an additional lift force suggests the possibility of high throughput deformability-induced particle classification and separation.<sup>26–28</sup> Deformation-induced lift forces will act in superposition with inertial lift forces to create modified lateral equilibrium positions that are dependent on particle deformability. Consequently, the lateral equilibrium position can then be used as the measure of particle deformability when the particle size is taken into account. Furthermore, the differences in lateral equilibrium position among cell types can be utilized for deformability-induced target cell enrichment by directing entrained target cells to separate designated outlets.

## Methods

### Cell preparation

Whole blood samples were drawn from healthy volunteers into venous blood collection tubes (BD Vacutainer®) containing 0.4 mL of trisodium citrate (13.2 g L<sup>-1</sup>), citric acid (4.8 g L<sup>-1</sup>) and dextrose (14.7 g L<sup>-1</sup>). Leukocytes were either purchased from the Center for AIDS Research Virology Core/BSL3 Facility or obtained by selectively lysing erythrocytes using RBC lysis buffer (eBioscience). HeLa cells (a cervical carcinoma cell line), MCF7 cells (a breast carcinoma cell line) and SAOS-2 (an osteosarcoma cell line) were cultured in the growth media suggested by American Type Culture Collection (ATCC™) and incubated at 37 °C in 5% CO<sub>2</sub> until near confluence. Breast cancer cells (modMCF7), representing a highly invasive phenotype,<sup>29</sup> were obtained by chemically modifying MCF7 cells with 100 nM 12-*O*-tetradecanoylphorbol-13-acetate (TPA) for 18–24 h.<sup>3</sup> For spiking experiments, blood and cancer cells were mixed to achieve a final ratio of 1 : 100 cancer cells to blood cells. Dilute cell solution with relatively low total number concentration (202 000 cells mL<sup>-1</sup>) was used for the experiment to avoid particle–particle interactions, leading to defocusing of particles at the expanding outlet and lower purity of collected samples.<sup>30</sup> Indeed, it was observed that more blood cells were directed towards the cancer outlet, contaminating the collected sample, when the cell solutions with higher number concentration (100 million cells mL<sup>-1</sup>) were introduced into the system (see ESI\_Movie 1†).

### Particle/capsule suspensions

Experiments with polydisperse elastic particles and viscous oil droplets with a wide range of elastic moduli and kinematic viscosity were conducted to isolate dominant contributions to lateral migration of particles. Particles/droplets were created by forming stable surfactant coated spheres in deionized water with 3% w/v Tween 80 (Fisher Chemical) through vigorously mixing two immiscible liquids (uncured polydimethylsiloxane (PDMS) polymer or silicone oils).<sup>31</sup> Interfacial tension between the two immiscible phases was kept uniform and small by controlling surfactant concentration (~0.5 mJ m<sup>-2</sup>), which is the reported value for a stabilized emulsion.<sup>32</sup> Moreover, the interface of droplets was considered to be saturated with the surfactant molecules since the molar concentration of Tween 80

in the solution (28 mM) was much higher than its critical micelle concentration (13 μM at 25 °C). Saturation of the surfactant molecules at the water/oil interface allows the no-slip boundary condition at the interface to be valid.<sup>33</sup> After curing, PDMS solid particle emulsions were centrifuged to collect microparticles whose diameters ranged between 2 and 30 μm.<sup>34</sup> Solid elastic particles made of PDMS and viscous oil droplets with a deformable interface are referred to as PDMS particles and viscous droplets, respectively. The deformability of PDMS particles was controlled by varying crosslinker density<sup>35</sup> while that of viscous oil capsules was controlled by choosing silicone oil with various kinematic viscosities (1 cSt <  $\nu$  < 1000 cSt, PDMS 200, Dow Corning). Young's moduli of microparticles were assumed to be identical to that of bulk PDMS specimens<sup>36</sup> and were directly measured (for 10 : 1–65 : 1 base to crosslinker ratios) with standard tensile tests (Instron 4111, elongation rate at 0.5 mm min<sup>-1</sup>) while those of samples with lower crosslinker density (74 : 1 and 80 : 1) were interpolated based on the aforementioned measurements. Young's moduli of PDMS particles were found to range from 0.5 to 1000 kPa (see ESI\_Figure 2(a)†).

### Inertial focusing of deformable particles/capsules and high speed imaging

We assayed the lateral equilibrium positions of PDMS particles, viscous oil droplets, red blood cells, peripheral blood mononuclear cells, and benign and metastatic cancer cells by individually injecting solutions through a single straight channel with high aspect ratio (*i.e.*,  $W : H \approx 1 : 2$ ). Micro-particle/cell containing samples were injected into the device with a syringe pump (Harvard Apparatus, PHD 20000) equipped with a 10 mL glass syringe (Hamilton) to sustain an overall flow rate,  $Q$ , ranging between 25 μL min<sup>-1</sup> and 450 μL min<sup>-1</sup>. The solution in a vertically oriented glass syringe was continuously agitated during injection in order to maintain a uniform concentration throughout the experiment. The loaded syringe was connected to 1/32 × 0.02" PEEK tubing (Upchurch Scientific) by a 1/2" luer stub (Instech Solomon) and tubing was secured in the punched inlet and outlet of the microfluidic device. High-speed microscopic images of inertially focused cells/particles were recorded downstream using a Phantom v7.3 high speed camera (Vision Research Inc.) and Phantom Camera Control software. All high speed images were taken using 1 μs exposure time and image intervals were varied according to the flow rate. The lateral equilibrium position ( $X_{eq}$ ) of individual particles/cells was determined by measuring the distance between the particle center and the channel wall ( $X_{eq}$  equal to 0 or 1 indicates that a particle was centered at the channel wall or centerline, respectively) with the aid of high-speed microscopy and image viewer software, Irfanview (see ESI\_Figure 1†). Particle/cell diameter,  $a$ , and lateral equilibrium position,  $X_{eq}$ , were determined with ±0.56 μm accuracy for each data point. More than 100  $X_{eq}$  data points for each individual particle/cell type were taken in order to obtain clear statistical insight. The maximum and average standard error for each averaged  $X_{eq}$  data point was found to be 0.07 and 0.01, respectively.

## Device design and fabrication

For cell classification we implemented a straight high aspect ratio channel ( $W = 38 \mu\text{m}$ ,  $H = 85 \mu\text{m}$  and  $L = 4.5 \text{ cm}$ ), consisting of one inlet with coarse filters and one outlet, in which particle/cells are inertially focused to two lateral focusing positions at a uniform  $z$ -plane. For cell enrichment we designed a deformability activated cell sorting (DACS) microfluidic device, which is composed of one inlet with coarse filters, a straight focusing channel ( $W = 40 \mu\text{m}$ ,  $H = 93 \mu\text{m}$  and  $L = 4.5 \text{ cm}$ ), a gradually expanding region, and 5 branched outlets with fluidic resistors (see Fig. 1(d)). The focusing channel length was designed to be 4.5 cm to ensure complete particle ordering as the critical channel length,  $L_f$ , required to focus smaller red blood cells ( $6 \mu\text{m} < a < 8 \mu\text{m}$ ), was found to range from 1.8 to 3.1 cm at  $R_c = 21$ .  $L_f$  was calculated by balancing the shear-gradient lift force with Stokes drag as we previously reported.<sup>18</sup> A gradually expanding region was empirically evaluated to maintain focused cells in the focusing streamline while enhancing the  $X_{eq}$  differences between cell types when compared to straight angled expansions (ESI\_Figure 3(c) and (d)†). The expanding region was designed by gradually increasing the angle between the channel wall and the flow direction by  $2^\circ$  per  $100 \mu\text{m}$ . Each outlet has a fluidic resistor (a serpentine channel) attached in order to minimize the flow ratio distortion due to any small variation in the fluidic resistance at the outlet (e.g. small variation in tubing length or small debris partially clogging one or more outlets).

The microfluidic devices were fabricated with conventional soft lithography techniques using PDMS. In brief, the mold was fabricated by spin-coating a negative photoresist (KMPR 1050, Microchem) on a 4" silicon wafer to obtain desired height of microfluidic channels (85 or 93  $\mu\text{m}$ ). PDMS (Sylgard 184, Dow Corning) was cast on to the prepared mold and degassed. Inlet and outlets of the devices were punched in the cured PDMS cast with a pin vice (Pin vise set A, Technical Innovation, Inc.) and bonded to slide glass using air plasma (Plasma Cleaner, Harrick Plasma).

## Enrichment of cancer cells spiked in peripheral blood

Blood cell suspensions spiked with cancer cells were injected into the DACS in order to separate and enrich cancer cells. Two different flow rates (corresponding to  $R_c = 21$  and 42) and two fluidic resistances were tested in order to examine the effect of flow rate and outlet resistance on enrichment. These values for Reynolds number,  $R_c$ , were determined based on  $X_{eq}$  and cancer cell yield data conducted in separate experiments (See ESI\_Figure 3(a) and (b)†). In the range tested the difference between blood and cancer cell equilibrium positions are maximized, while maintaining high yield and throughput. A mixture of cancer and blood cells were prepared by spiking modMCF7 or SAOS-2 cells into dilute whole blood or mononuclear blood cells at a ratio of 1 to 100. The fractions collected from blood (two outer) and cancer (three inner) outlets were combined and used for flow cytometry analysis (BD FACSCalibur, BD Bioscience), performed for quantitative evaluation of DACS target cell enrichment ability. Cancer cells were fluorescently labeled with 2  $\mu\text{M}$  Calcein AM (Invitrogen™) prior to preparing the cell mixture, whereas leukocytes were labeled with anti-CD45 PerCP

(BD Bioscience). The intensities of Calcein AM (green fluorescence) and PerCP were measured using the detector FL1 and FL3, respectively, to distinguish cancer cells and leukocytes. The gates were set for statistical analysis such that more than 96% of the population of stained leukocytes (FL3) or cancer cells (FL1) is counted in the gated regions as determined from the intensity measurements of individual cell types. The enrichment ratio,  $ER = \frac{(Cancer/Blood)_{outlet}}{(Cancer/Blood)_{inlet}}$ , was determined by comparing

the ratios of blood and cancer cells at designated outlets, obtained using FACS analysis. In addition, cancer and blood cell yield was determined by flowing blood cells and cancer cells separately through the device and counting the number of cells collected at each outlet using a Coulter Counter (Z2TM Coulter Counter®, Beckman Coulter).

## Global gene expression and cell viability

We assessed whether shear stress acting on cells flowed through the inertial microfluidic device would result in altered global gene expression. First, MCF7 cells were harvested from the flask grown under normal conditions following standard subculturing protocols. Half of the cell population was saved in microcentrifuge tubes and labeled as control samples (C1–C4). The control samples were kept at room temperature (not under growth conditions) while the remaining MCF7 cells harvested from the same flask were flowed through the DACS device at  $R_c = 21$  for 3 h. The processed cells were collected in microcentrifuge tubes and labeled as flow samples (F1–F4). To assay long-term changes in gene expression, a portion of the control and flow samples were separately cultured under normal growth conditions in 12 well plates, harvested after 24 h and labeled as 24 h control (24 h C1–C4) and flow (24 h F1–F4) samples, respectively. To reduce false-positive results, four replicates were arrayed from two independent cultures of MCF-7 cells performed on separate days per each experimental condition (e.g., control, flow, control 24 h and flow 24 h). Live/dead assay using Calcein AM and Ethidium homodimer-2 (Invitrogen) was performed for subpopulations of each experimental condition, prior to the microarray analysis, in order to determine the viability of processed cancer cells following established protocols. The number ratio between live and dead cells was determined by counting stained cells in fluorescence images ( $N = 10$ ) taken at random locations. Total RNA isolation was done using TRIzol® Reagent (Invitrogen) followed by RNeasy MinElute Cleanup (Qiagen). RNA from individual samples was prepared for cDNA synthesis and hybridization to Affymetrix GeneChip® Human Gene 1.0 ST arrays and gene expression of over 28 000 gene probe sets was measured. Eluted total RNAs were quantified and adjusted to a final concentration of 100 ng. cDNA was synthesized following the WT Expression Kit protocol (Ambion). cDNA was fragmented and labeled using the GeneChip WT Terminal Labeling and Hybridization Kit (Affymetrix). Finally 2.5  $\mu\text{g}$  of cDNA was hybridized at 45 °C with rotation for 18 h (Affymetrix GeneChip Hybridization Oven 640) to an Affymetrix GeneChip Human Gene 1.0 ST Array as per the manufacturer's instructions (Affymetrix, Inc.). The GeneChip arrays were washed and then stained with streptavidin–phycoerythrin on an Affymetrix Fluidics Station 450,

followed by scanning on an Affymetrix GeneChipScanner 3000 7G. Results (CEL files) were normalized with MAS5 in dChip software<sup>37</sup> with the average modeling method and 5th percentile of region as background subtraction with median probe intensity brightness and call percent as the baseline array (sample # F3). The MAS5-normalized data were further analyzed with dChip.<sup>37</sup> Annotations and sequences of probes on the Affymetrix® Gene Chip® Human 1.0 ST Array were based on release version 30 (January 2010). The unsupervised learning method of average linkage hierarchical clustering (HC) with the Euclidean distance measure was used to cluster the microarray samples on the basis of their gene expression profiles in dChip. The most highly varying genes were selected by restricting the unsupervised analysis to genes with coefficients of variance between 0.38 and 1000. This resulted in 364 Affymetrix-annotated genes (2035 probe sets), which will be referred to as the most varying genes. Differentially expressed gene lists were generated by comparing the experimental group (F or 24 h F) to the baseline (C or 24 h C) using the following parameters: (i) two sample *t*-test with  $p < 0.05$ , (ii) absolute expression value of fold change between samples greater than 2 with lower 90% confidence interval, and (iii) absolute difference between samples greater than 100. Furthermore, Ingenuity Pathways Analysis (Ingenuity® Systems) software using the Benjamini–Hochburg multiple testing correction *p*-value was used to determine significant KEGG canonical pathways, novel network pathways and functional enrichment groups disrupted within the sets of differentially expressed genes. The settings applied for pathway/function analyses include (i) general settings: direct and indirect relationships; (ii) data sources: all; (iii) species: human only; (iv) tissues and cell lines: breast cancer cell lines only; with (iii) and (iv) set to filter molecules and relationships.

## Results and discussion

### Lateral equilibrium position is a function of particle viscoelastic properties

The lateral equilibrium positions ( $X_{eq}$ ) of particles and viscous droplets strongly depend on particle size and viscosity (see Fig. 2(a and b)). Compared to the baseline equilibrium positions of rigid PDMS particles (elasticity over a range of 0.5–1000 kPa, raw data can be found in ESI\_Figure 2(a)†) deformable droplets occupied equilibrium positions much closer to the channel centerline (Fig. 2(c)). Additionally, the droplets were observed to shift towards the channel-center as viscosity decreased (from 1000 to 5 cSt). For lower viscosities, droplets were observed to adopt more deformed shapes at steady state (Fig. 2(d)) which is associated with increased deformation-induced lift.<sup>19,21,23,25</sup> These data are consistent with a lateral force that is inversely related to droplet viscosity ratio in general agreement with previous theoretical and computational studies.<sup>22,38,39</sup> Moreover, in agreement with previous computational studies, the shape of droplets with lower viscosity ( $\lambda < 10$ ) exhibited a larger curvature near the channel wall, suggesting that the surface of the droplet near the wall experiences larger stresses.<sup>39</sup> Note that the  $X_{eq}$  of oil droplets with  $\lambda = 970$  was found to be much closer to the channel centerline than that of solid particles although the droplets exhibited an undistorted, spherical shape similar to that of elastic

solid particles. This could be attributed to the fact that the interface of oil droplets is a non-solid boundary, allowing additional dynamics that could contribute to differences in lateral drift, such as internal fluid circulation and tank-treading motion of the surfactant molecules at the interface, which are not present for solid particles.

Interestingly, as the viscosity decreases below 5 cSt ( $\lambda < 4.6$ ), the lateral equilibrium position again moved closer to the channel wall (Fig. 2(d)) despite the similarity in the droplet shape. This counter intuitive phenomenon may have its origins in a shift in the direction of deformability-induced migration as

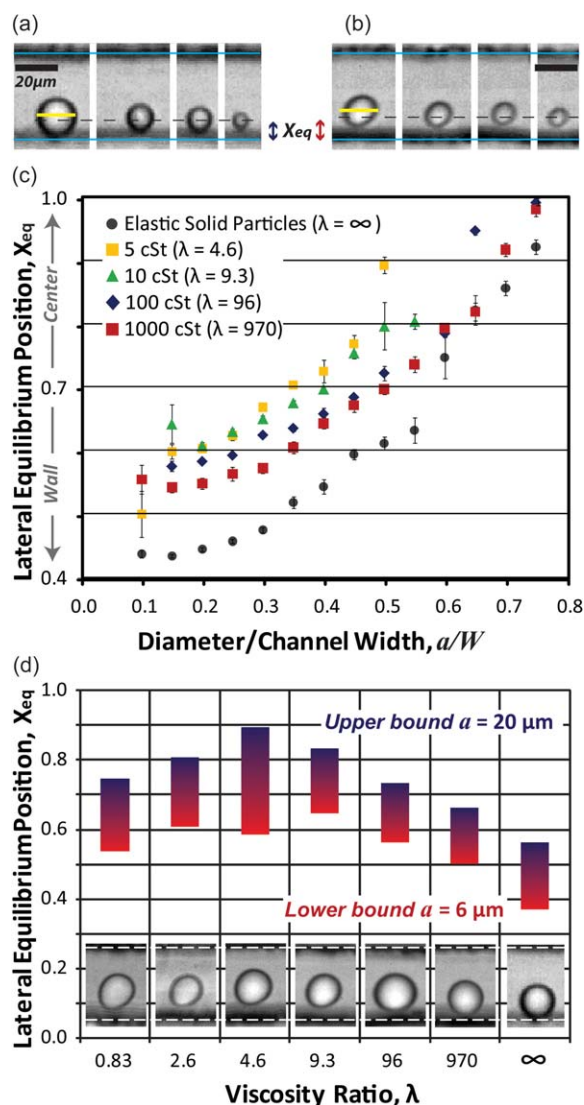


**Fig. 2** Particle viscoelastic properties affect lateral equilibrium position. High-speed microscopic images of (a) elastic solid particles (*i.e.*, relatively rigid) and (b) viscous oil droplets (*i.e.*, highly deformable) of various sizes are shown.  $X_{eq}$  for viscous oil droplets and elastic particles varies as a function of (c) particle diameter to channel width,  $a/W$ , and (d) viscosity ratio,  $\lambda$ . Error bars in (c) indicate the standard error and  $\lambda$  is the ratio between the dynamic viscosity of oil and water at 25 °C. Bars in part (d) represent the range of equilibrium position measurements for particles and oil droplets whose diameters range from 6 μm (bottom) to 20 μm (top). All data points were obtained by flowing particulates at  $Re = 21$ .

a function of internal to external viscosity ratio,  $\lambda$ . This shift in direction has been previously explored theoretically for buoyant viscous drops moving near a wall<sup>39</sup> and a viscous drop in Poiseuille flow at finite Reynolds number.<sup>25</sup> In this previous study, viscous drops migrated towards the wall for  $\lambda = 2$  and towards the centerline for  $\lambda = 8$ .<sup>25</sup> Mortazavi and Tryggvason argued that this phenomenon could be explained since droplets with higher viscosity ( $\lambda = 8$ ) more effectively slow down the surrounding flow in between the droplet and the channel wall, thus lower viscosity droplets ( $\lambda = 2$ ) have a thinner lubrication layer, yielding smaller lateral equilibrium positions.<sup>25</sup> Further studies will be needed to clarify the definitive cause of this direction change in lateral migration.

### Lateral equilibrium position of cells can be used for classification of cell type

Cells migrated to positions closer to the channel centerline than rigid particles, behaving in a similar manner to viscous droplets. Cell diameters for all cancer cell lines tested were measured to be larger than blood cells, and the size of MCF7 cells was found to be larger than that of HeLa cells in good agreement with previous reported values for such cells.<sup>40,41</sup> As shown in Fig. 3,  $X_{eq}$  for cells, including blood (erythrocytes and leukocytes), carcinoma (HeLa and MCF7) and osteosarcoma (SAOS-2) cells, was found to follow a comparable trend to that of viscous droplets ( $4.6 < \lambda < 970$ ). Although the mechanical properties of a few cell lines (HeLa, MCF7 and MCF10A) considered in this study were previously reported to be similar to the elasticity of PDMS particles used in the present study,<sup>42,43</sup> these measurements were done using atomic force microscopy of cells adhered on surfaces. In our system we found these cell lines to behave more similarly to viscous droplets, rather than rigid objects with the reported elasticity. This disagreement could originate from the fact that the previous measurements were done with adherent cells whereas individual freely rotating cells in suspension were observed in current experiments. The experimental results are also in agreement with the previous report, showing that the viscous properties of cells dominate under high frequency perturbation.<sup>44</sup> Notably, breast cancer cells with increased metastatic potential (*i.e.* modMCF7 cells) were found to migrate even closer to the centerline than benign breast cancer cells (MCF7) despite the similarity in cell diameter range (Fig. 3(a)). In general, cancer cells were also easily distinguishable from blood cells based on their size and equilibrium positions. A histogram of  $X_{eq}$  for leukocytes, breast cancer cells and osteosarcoma cells illustrates that more than 97% of cancer cells were found to have  $X_{eq}$  greater than 0.6 (see Fig. 3(b)). This indicates that successful gating ( $0.6 < X_{eq}$ ) would have a great potential to enable cancer cell detection with high sensitivity and specificity in a mixed dilute blood sample (for example in detection of circulating tumor cells). It is still unclear whether the physical properties and size of CTCs will correspond with those of cultured cancer cell lines, although reports have identified that cell size and deformability can be used as a biomarker for metastatic cells.<sup>1,3,4,45</sup> We assembled a receiver operating characteristic curve from these data for detecting cancer cells amongst a blood cell population and determined the area under the curve (AUC) using the empirical method.<sup>46</sup> A high AUC greater than 0.91 was

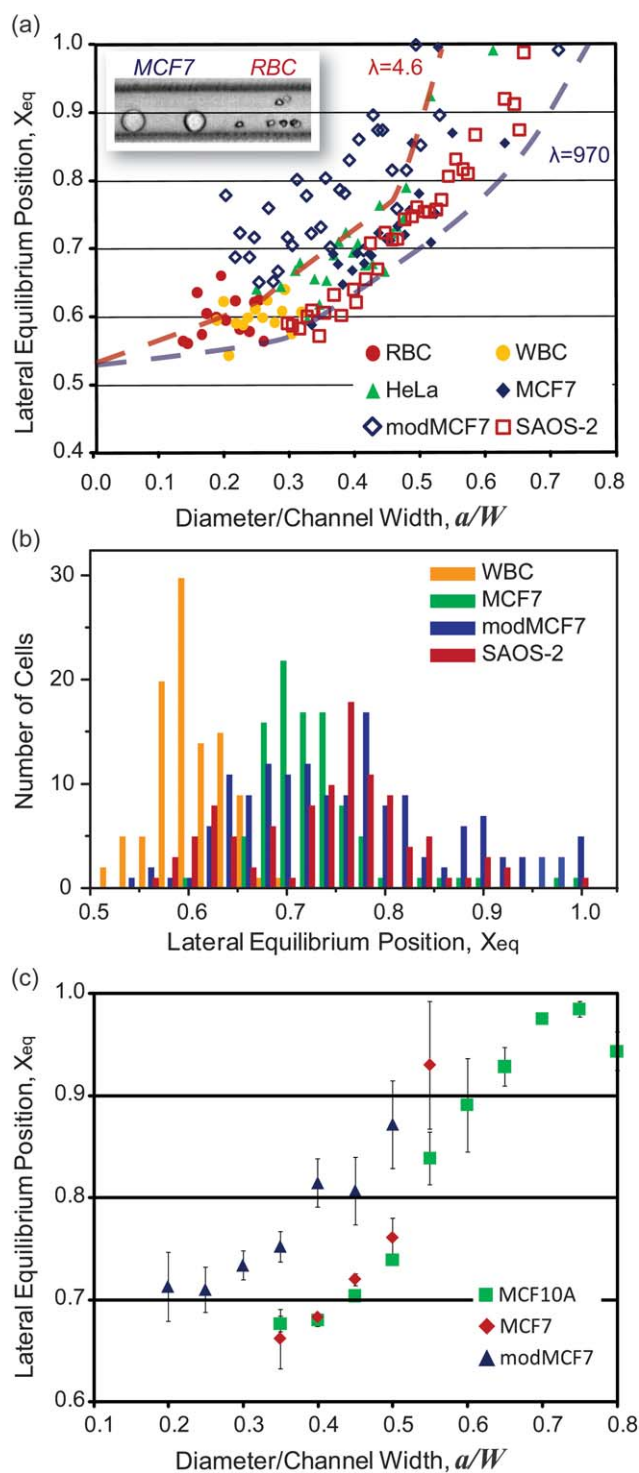


**Fig. 3** Lateral equilibrium positions,  $X_{eq}$  and size of cells is indicative of cell type. (a)  $X_{eq}$  of blood cells, carcinoma, and osteosarcoma cells is plotted as a function of cell diameter to channel width ratio,  $a/W$  at  $R_c = 21$ . (b) Histogram of  $X_{eq}$  for leukocytes, MCF7 cells, modified MCF7 cells and SAOS-2 cells at  $R_c = 21$ . Using a cut-off for  $X_{eq}$  at 0.6 yields high sensitivity and specificity classification of cancer cells amongst leukocytes (see ESI\_Figure 4†). (c) Averaged  $X_{eq}$  of normal (MCF10A), benign (MCF7) and malignant breast epithelial cells (modMCF7) illustrates the potential for classification of tumor cell invasiveness. Error bars in (c) indicate the standard deviation.

attained for all cancer cell lines tested (see ESI\_Figure 4†), suggesting that the current technique would be useful in identifying cancer cells in blood with high sensitivity and specificity.

Moreover, the lateral equilibrium position of malignant cancer cells (modMCF7) was found to be distinctively different from those of benign cancer cells (MCF7) and normal tissue cells (MCF10A) from the same origin (see Fig. 3(c)), indicating the potential to enable determination of cancer invasiveness or stage from disaggregated biopsy samples. This is in good agreement with previous reports showing that modMCF7 cells are much more deformable than their benign or healthy counterparts.<sup>3</sup> Additionally, the technique holds promise for other cases where deformability changes accompany phenotypic changes, for example in assaying the level of leukocyte activation<sup>7,8</sup> or degree of embryonic stem cell differentiation.<sup>47</sup> A combination of cell size and  $X_{eq}$  measurements may provide a unique cellular signature, allowing automatic target cell enumeration through image-based or other optical detection approaches. Furthermore, the simplicity of the device (a single rectangular channel) is expected to allow the system to be easily parallelized in order to further enhance the throughput.<sup>18</sup>

#### Passive label-free enrichment of spiked cancer cells in dilute whole blood

Using the significant differences in lateral equilibrium position between cancer and blood cells we conducted label-free enrichment and collection of these cells (Fig. 4(a)). Fig. 4(b) shows the cellular components at the inlet and the fractions from the blood and cancer outlets. The maximum enrichment ratio for both modMCF-7 and SAOS-2 cells was found at  $R_c = 21$  with modified fluidic resistances at the blood outlets (0.1% reduction in overall fluidic resistance). In agreement with  $X_{eq}$  measurements (Fig. 3(a)), more deformable metastatic breast cancer cells (modMCF7) were found to have a better enrichment ratio than osteosarcoma cells (SAOS-2). Metastatic breast cancer cells were enriched by a factor of 5.4 with 96% recovery of target cells at the collection outlets while osteosarcoma cells were enriched by  $3.2\times$  with 97% yield. Note that the reported values are the conservative, lower limit of the enrichment ratio as the signal from double stained cells exhibiting high intensity levels at both FL1 and FL3 was excluded in the enrichment ratio determination. This signal from double stained cells could originate from leukocytes bound to cancer cells deemed immunologically foreign since the blood sample and cancer cells were obtained from immunologically different subjects (e.g., T-cell mediated immune response<sup>48</sup>).

The throughput of a single device is  $\sim 22\,000$  cells  $\text{min}^{-1}$  when the device is operated at  $R_c = 42$ . Although the current throughput is considerably slower than conventional rare cell enrichment systems, the approach is label-free and does not require complex, additional electrical/optical components as other active, label-free target cell separation techniques do.<sup>49</sup> Additionally, throughput can be further improved by parallelizing the device as previously shown by our research group.<sup>50</sup> With parallelization of 45 single-devices, 1 mL of RBC-lysed blood ( $\sim 8$  million WBCs) is expected to be processed within 8 min. Moreover, owing to the simplicity of the device (e.g. a single-layer device with one input and no additional external

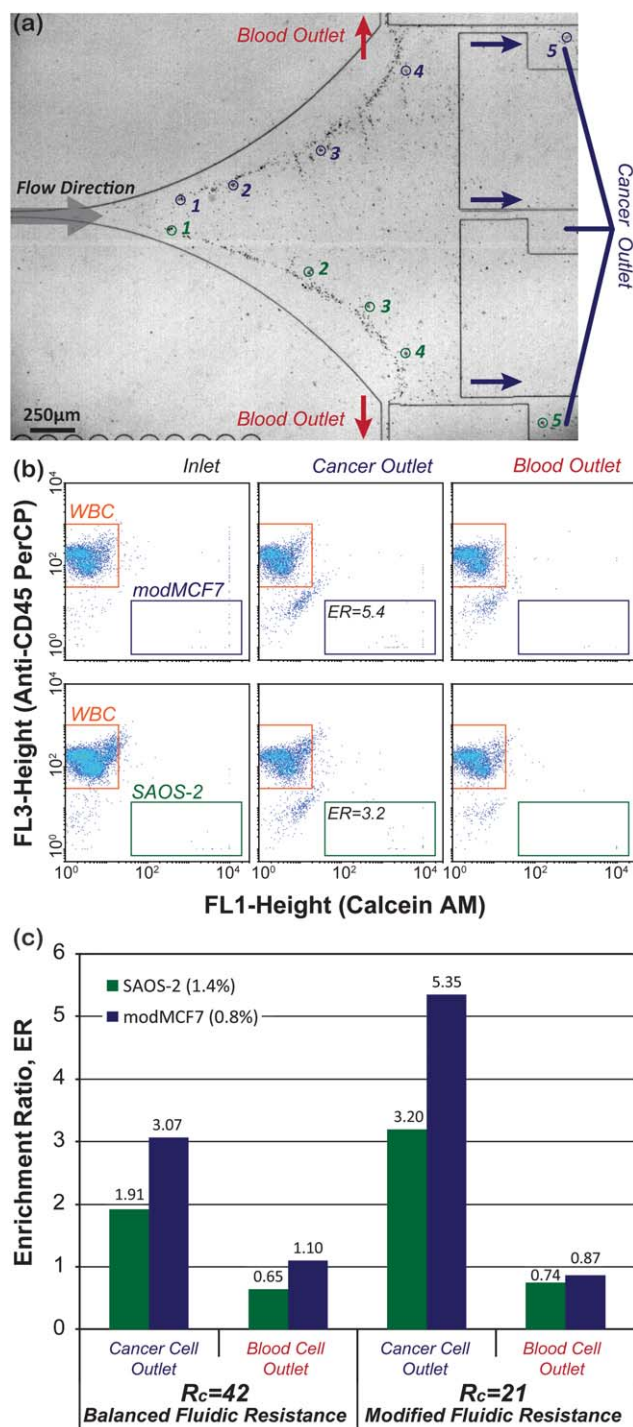


**Fig. 4** Passive label-free deformability-activated cell enrichment. (a) An image of our separation outlet is shown, constructed from sequences of high-speed microscopy images with a time interval of 33 ms. Red and blue arrows indicate the outlets for blood cells and enrichment of cancer cells, respectively. Individual cancer cells separated from the mixture are marked with blue and green circles. (b) Flow cytometry data show that the cell populations in the initial sample and those collected from cancer and blood outlets are different. The initial fraction of the cancer cells (modMCF7 and SAOS-2) to leukocytes was 0.8% and 1.4%, respectively. (c) A comparison of enrichment ratios for modMCF7 and SAOS-2 cells at varied flow conditions is shown.

force requirements) and high yield, the system can be easily cascaded in series in a similar way to the system recently reported by Sim *et al.*<sup>51</sup> in order to achieve higher levels of enrichment without significant sample loss. We also note that the system is very robust, operating stably for >3 h without clogging or intervention due to our innovations in microfluidic design (including low shear transitions that prevent cell rupture and clogging and high-impedance outlets which maintain flow rate uniform with small clogs). Immediate promising application areas for the system include as a simple processing unit integrated upfront to state-of-the-art image based target cell detection systems<sup>9,45</sup> or FACS in order to enhance the overall throughput by reducing the RBC/WBC background.

### Gene expression and cell viability is not significantly affected by inertial separation

The overall gene expression profile of MCF7 cells before and after flow through the system showed only minor changes and the processed cells remained highly viable and proliferated for over a week (ESI\_Figure 5†). Unsupervised clustering using the

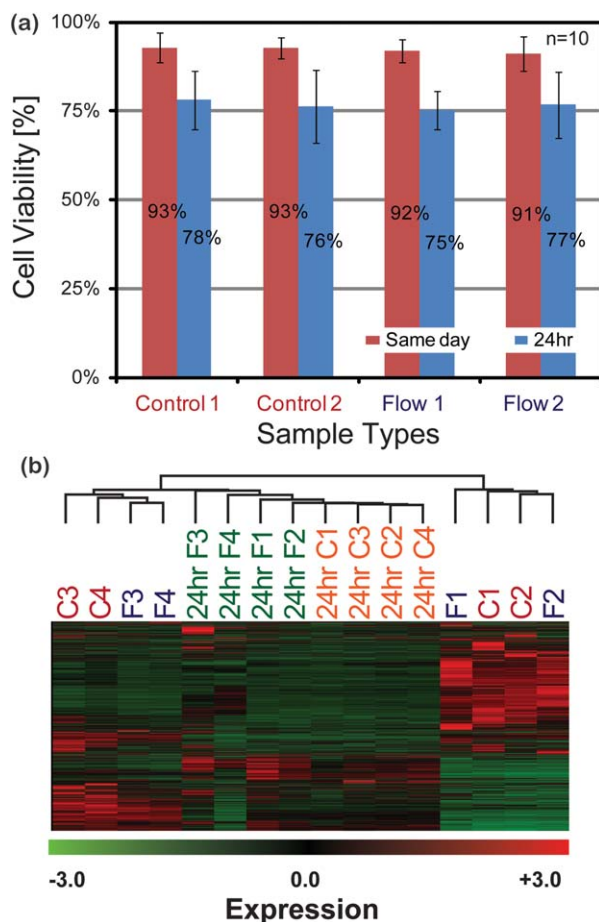


**Fig. 5** Inertial focusing does not significantly affect cell viability and gene expression. (a) Viability tests show that cells flowed through the device remain highly viable similar to control cells not flowed through the system. (b) Unsupervised hierarchical clustering of microarray data for MCF7 cells for 8 control and 8 flow conditions (number of annotated genes = 364) illustrates that the processed cells do not have distinct global gene expression compared to control samples.

364 most varying annotated genes (2035 probe sets) was performed to determine whether cells flowed through the device have globally distinct gene expression profiles since (i) not all of the 2035 probe sets have annotations and (ii) the same clustering pattern seen in the 364 gene list is observed with the 2035 gene list. Hierarchical clustering showed that control and flow samples (C and F) and 24 h samples were clustered together (see Fig. 5(b)), indicating that the gene expression profiles for processed MCF7 cells were not globally distinct from the control samples. Interestingly, but unrelated to processing in the device, the 24 h C/24 h F samples clustered closely together, suggesting an effect due to culture prior to analysis. Moreover, gene filtering between control (C1–C4) and flow (F1–F4) samples collected at the same day of processing using a *t*-test ( $p < 0.05$ ) and the fold-change criterion (2 fold-change) showed that no single gene was differentially expressed between those samples. However, gene filtering analysis (2 fold-change) of 24 h samples revealed one probe set without an annotated gene name that was up-regulated in 24 h flow samples compared to 24 h control samples.

Temporal differences revealed 46 and 69 probe sets corresponding to 27 (gene list 1) and 25 (gene list 2) Affymetrix-annotated genes, that were differentially expressed between C and 24 h C, and F and 24 h F, respectively. Of these, twenty-seven probe sets/16 annotated genes (gene list 3) overlapped between C versus 24 h C and F versus 24 h F. These three gene lists were used for hierarchical clustering dendrograms (ESI\_Figure 6†) and imported into the Ingenuity program for pathway analysis. Pathway analysis revealed that aminoacyl-tRNA biosynthesis, glycine, threonine and serine metabolism, and alanine and aspartate metabolism were significant canonical pathways in both the C vs. 24 h C and F vs. 24 h F samples. Aryl hydrocarbon receptor signaling was a unique canonical pathway in the C vs. 24 h C samples only (ESI\_Figure 7†). No significant, non-canonical network pathways or functional enrichment groups were revealed in the C vs. 24 h C or F vs. 24 h F comparisons.

We conclude that there are no significant alterations caused by initially flowing cells through the device as evidenced by no statistical differences in gene expression at 2-fold change. Only a limited number of genes in the C vs. 24 h C and F vs. 24 h F samples have altered expression after 24 h of incubation. 27 total/16 annotated genes were in common between C vs. 24 h C and F vs. 24 h F samples, indicating that the major subset of the gene expression differences are independent of flow. An important assessment of the temporal effects of flow can be seen in pathway alterations. There is only one pathway difference between C vs. 24 h C and F vs. 24 h F samples: aryl hydrocarbon receptor signaling which is a type of toxic and carcinogenic exposure response. In C samples, 2/3 genes in this pathway were down-regulated. The remaining 3 pathways are the same for C vs. 24 h C and F vs. 24 h F, further proof of minimal impact of the long-term effects of flowing cells through the device.

Furthermore, the expression profiles of potential genes of interest for development of targeted anticancer therapeutics (MDR1, MRP, LRP, p53)<sup>52</sup> or breast cancer prognostic and clinical stage forecasting (errB-2)<sup>53,54</sup> were not shown to be differentially expressed between control and experimental samples, which does not rule out the use of this approach to isolate cells for assessment of anticancer drug efficacy and identification of a personalized therapy.

## Conclusions

We have developed a microfluidic device for passive label-free cell classification and enrichment that uniquely uses cell size and deformability as distinguishing markers. It has been found that suspended cells behave much like viscous droplets moving closer to the channel centerline than rigid particles. Consequently, more deformable and larger metastatic cancer cells were observed with lateral equilibrium positions closer to the channel centerline than blood cells, benign cancer and normal tissue cells from the same origin. Given these results, clinical and research instruments are now possible for high-throughput cell classification using cell deformability as a biomarker. Moreover, using lateral equilibrium position differences we adapted the system to conduct label-free cell enrichment based on cell size and deformability, which may have immediate use in lowering the WBC background for imaging-based cell detection. Further improvements in microfluidic design and sequential processing leading to improved enrichment ratios are expected to increase the application areas for this approach. Importantly, little change in the global gene expression profiles of processed cells indicates that the proposed technique is appropriate for clinical and research applications in which gene expression analysis, or establishment of *in vitro* culture are desired. Taking advantage of cellular-scale hydrodynamics in inertial flows, the presented technique has practical potential for cost-effective cell separation and high-throughput deformability measurements of clinical and biological importance.

## Acknowledgements

The authors thank Jong-se Park PhD and Professor Thomas H. Hahn PhD for the standard tensile tests, Dennis J. Yoon and Professor Daniel T. Kamei PhD for instructing Coulter measurements, Eric J. Tsang and Professor Patricia A. Zuk PhD for providing osteosarcoma cells, and Karin Chen M.D., Jamie Powers M.D. and UCLA CFAR virology laboratory for providing de-identified blood samples. We also thank Lance Hultin and Marianne Chow for assisting with FACS analysis. Flow cytometry was performed in the UCLA Jonsson Comprehensive Cancer Center and Center for AIDS Research Flow Cytometry Core Facility that is supported by the National Institutes of Health Awards CA-16042 and AI-28697, by the Jonsson Cancer Center, the UCLA AIDS Institute and the UCLA school of Medicine. This work was partially supported by the National Science Foundation under grant 0930501.

## References

- S. Suresh, *Acta Biomater.*, 2007, **3**, 413–438.
- S. Suresh, J. Spatz, J. Mills, A. Micoulet, M. Dao, C. Lim, M. Beil and T. Seufferlein, *Acta Biomater.*, 2005, **1**, 15–30.
- J. Guck, S. Schinkinger, B. Lincoln, F. Wottawah, S. Ebert, M. Romeyke, D. Lenz, H. M. Erickson, R. Ananthakrishnan, D. Mitchell, J. Kas, S. Ulvick and C. Bilby, *Biophys. J.*, 2005, **88**, 3689–3698.
- S. Cross, Y. Jin, J. Rao and J. Gimzewski, *Nat. Nanotechnol.*, 2007, **2**, 780–783.
- M. Brandão, A. Fontes, M. Barjas-Castro, L. Barbosa, F. Costa, C. Cesar and S. Saad, *Eur. J. Haematol.*, 2003, **70**, 207–211.
- N. Mohandas and S. Shohet, *Curr. Top. Hematol.*, 1978, **1**, 71.
- E. Drost and W. MacNee, *Eur. J. Immunol.*, 2002, **32**, 393–403.
- A. Skoutelis, V. Kaleridis, C. Gogos, G. Athanassiou, Y. Missirlis and H. Bassaris, *Cytokine*, 2000, **12**, 1737–1740.
- S. Nagrath, L. Sequist, S. Maheswaran, D. Bell, D. Irimia, L. Ulkus, M. Smith, E. Kwak, S. Digumarthy and A. Muzikansky, *Nature*, 2007, **450**, 1235–1239.
- G. Lee and C. Lim, *Trends Biotechnol.*, 2007, **25**, 111–118.
- K. Ward, W. Li, S. Zimmer and T. Davis, *Biorheology*, 1991, **28**, 301.
- R. Hochmuth, *J. Biomech.*, 2000, **33**, 15–22.
- M. Rosenbluth, W. Lam and D. Fletcher, *Biophys. J.*, 2006, **90**, 2994–3003.
- M. Lekka, P. Laidler, D. Gil, J. Lekki, Z. Stachura and A. Hryniewicz, *Eur. Biophys. J.*, 1999, **28**, 312–316.
- N. Wang and D. Ingber, *Biochem. Cell Biol.*, 1995, **73**, 327–336.
- D. Di Carlo, *Lab Chip*, 2009, **9**, 3038–3046.
- J. Matas, J. Morris and E. Guazzelli, *J. Fluid Mech.*, 2004, **515**, 171–195.
- S. C. Hur, H. T. K. Tse and D. Di Carlo, *Lab Chip*, 2010, **10**, 274–280.
- C. K. W. Tam and W. Hyman, *J. Fluid Mech.*, 1973, **59**, 177–185.
- L. Leal, *Annu. Rev. Fluid Mech.*, 1980, **12**, 435–476.
- S. K. Doddi and P. Bagchi, *Int. J. Multiphase Flow*, 2008, **34**, 966–986.
- P. Chan and L. Leal, *J. Fluid Mech.*, 1979, **92**, 131–170.
- M. Abkarian and A. Viallat, *Biophys. J.*, 2005, **89**, 1055–1066.
- J. Magnaudet, S. Takagi and D. Legendre, *J. Fluid Mech.*, 2003, **476**, 115–157.
- S. Mortazavi and G. Tryggvason, *J. Fluid Mech.*, 2000, **411**, 325–350.
- M. Chabert and J. Viovy, *Proc. Natl. Acad. Sci. U. S. A.*, 2008, **105**, 3191.
- M. Faivre, M. Abkarian, K. Bickraj and H. Stone, *Biorheology*, 2006, **43**, 147–159.
- H. W. H. Hou, A. A. S. B. Bhagat, A. G. L. Chong, P. M. Mao, K. S. W. Tan, J. Han and C. T. Lim, *Lab Chip*, 2010, **10**, 2605–2613.
- M. D. Johnson, J. A. Torri, M. E. Lippman and R. B. Dickson, *Exp. Cell Res.*, 1999, **247**, 105–113.
- W. Lee, H. Amini, H. Stone and D. Di Carlo, *Proc. Natl. Acad. Sci. U. S. A.*, 2010, **107**, 22413–22418, DOI: 10.1073/pnas.1010297107.
- D. Di Carlo, J. Edd, D. Irimia, R. Tompkins and M. Toner, *Anal. Chem.*, 2008, **80**, 2204–2201.
- P. De Gennes, F. Brochard-Wyart and D. Quéré, *Capillarity and wetting phenomena: drops, bubbles, pearls, waves*, Springer Verlag, 2004.
- R. Dagastine, R. Manica, S. Carnie, D. Chan, G. Stevens and F. Grieser, *Science*, 2006, **313**, 210.
- T. Svedberg and H. Rinde, *J. Am. Chem. Soc.*, 1924, **46**, 2677–2693.
- M. Ochsner, M. R. Dusseiller, H. M. Grandin, S. Luna-Morris, M. Textor, V. Vogel and M. L. Smith, *Lab Chip*, 2007, **7**, 1074–1077.
- R. Dingreville, J. Qu and M. Cherkaoui, Effective elastic modulus of nano-particles, *Proceedings, 9th International Symposium on Advanced Packaging Materials: Processes, Properties and Interfaces*, IEEE-Wiley, 2004.
- C. Li and W. Wong, *The Analysis of Gene Expression Data*, 2003, 120–141.
- A. J. Griggs, A. Z. Zinchenko and R. H. Davis, *Int. J. Multiphase Flow*, 2007, **33**, 182–206.
- W. Uijttewaala, E. Nijhof and R. Heethaar, *Phys. Fluids A*, 1993, **5**, 819.
- G. Gobert and H. Schatten, *J. Electron Microsc.*, 2000, **49**, 539.
- K. Rafferty, *Virchows Arch. B*, 1986, **50**, 167–180.
- S. Leporatti, D. Vergara, A. Zacheo, V. Vergaro, G. Maruccio, R. Cingolani and R. Rinaldi, *Nanotechnology*, 2009, **20**, 055103.
- Q. Li, G. Lee, C. Ong and C. Lim, *Biochem. Biophys. Res. Commun.*, 2008, **374**, 609–613.
- B. D. Hoffman and J. C. Crocker, *Annu. Rev. Biomed. Eng.*, 2009, **11**, 259–288.
- D. Marrinucci, K. Bethel, M. Luttggen, R. Bruce, J. Nieva and P. Kuhn, *Archives of Pathology and Laboratory Medicine*, 2009, **133**, 1468–1471.
- T. Lasko, J. Bhagwat, K. Zou and L. Ohno-Machado, *Journal of Biomedical Informatics*, 2005, **38**, 404–415.
- F. Chowdhury, S. Na, D. Li, Y. Poh, T. Tanaka, F. Wang and N. Wang, *Nat. Mater.*, 2009, **9**, 82–88.
- M. Sayegh and L. Turka, *N. Engl. J. Med.*, 1998, **338**, 1813.
- D. Gossett, W. Weaver, A. Mach, S. Hur, H. Tse, W. Lee, H. Amini and D. Di Carlo, *Anal. Bioanal. Chem.*, 2010, **397**, 3249–3267.
- A. J. Mach and D. Di Carlo, *Biotechnol. Bioeng.*, 2010, **107**, 302–311.
- T. Sim, K. Kwon, J. Park, J. Lee and H. Jung, *Lab Chip*, 2011, **11**, 93–99.
- Z. Duan, D. Lamendola, Y. Duan, R. Yusuf and M. Seiden, *Cancer Chemother. Pharmacol.*, 2005, **55**, 277–285.
- C. Fan, D. Oh, L. Wessels, B. Weigelt, D. Nuyten, A. Nobel, L. van't Veer and C. Perou, *N. Engl. J. Med.*, 2006, **355**, 560.
- M. West, C. Blanchette, H. Dressman, E. Huang, S. Ishida, R. Spang, H. Zuzan, J. Olson, J. Marks and J. Nevins, *Proc. Natl. Acad. Sci. U. S. A.*, 2001, **98**, 11462.